

Large-Scale Multi-Hypotheses Cell Tracking Using Ultrametric Contours Maps

Jordão Bragantini Merlin Lange Loïc Royer
Chan Zuckerberg Biohub

jordao.bragantini, merlin.lange, loic.royer@czbiohub.org

arXiv:2308.04526v1 [cs.CV] 8 Aug 2023

Abstract

In this work, we describe a method for large-scale 3D cell-tracking through a segmentation selection approach. The proposed method is effective at tracking cells across large microscopy datasets on two fronts: (i) It can solve problems containing millions of segmentation instances in terabyte-scale 3D+t datasets; (ii) It achieves competitive results with or without deep learning, which requires 3D annotated data, that is scarce in the fluorescence microscopy field. The proposed method computes cell tracks and segments using a hierarchy of segmentation hypotheses and selects disjoint segments by maximizing the overlap between adjacent frames. We show that this method achieves state-of-the-art results in 3D images from the cell tracking challenge and has a faster integer linear programming formulation. Moreover, our framework is flexible and supports segmentations from off-the-shelf cell segmentation models and can combine them into an ensemble that improves tracking. The code is available <https://github.com/royerlab/ultrack>.

1 Introduction

Tracking cells in terabyte-scale time-lapse volumetric image datasets of developing organisms acquired with the latest generation of light-sheet microscopes [19, 22, 54] is still an open problem. This conceptual and practical challenge involves segmenting individual cells and reconstructing their trajectories and lineages across multiple rounds of cell divisions. The scale of the data hinders the application of computationally intensive algorithms as these datasets easily contain thousands to millions of segmentation instances. Moreover, the lack of 3D ground-truth annotations also limits the application and performance of deep learning (DL) and other machine learning methodologies.

Methods usually tackle the problem in two different steps: computing the segmentation (or detection) and linking the previously detected instances given an association score. These methods can employ off-the-shelf segmentation models [52, 55, 41], and might use association scores from hand-crafted features [27]. However, segmentation

mistakes undermine the association score, harming the final tracking result. Because state-of-the-art segmentation methods are based on deep learning and require hard-to-obtain annotated data, their accuracy is greatly impaired when annotations are not available.

More recent methods based on flow-field estimation [16, 17, 56, 28, 18] circumvent these limitations by avoiding segmentation altogether and estimating the position and motion of cells between frames, relying only on a marker in the center of each cell and a link between the same cell and their divisions in adjacent frames. The association score is computed through the motion estimation. This kind of supervision requires much less effort than annotating volumetric segmentation instances.

Rather than avoiding segmentation, other approaches leverage the spatial information and compute the cell segments and their tracks jointly by modeling the cell nuclei as a mixture of Gaussians [2, 51], computing multiple segmentation hypotheses using ellipsoid fitting on their contours [59], or formulating the splitting and linking of regions (*i.e.* cells) in the image as a graph-cut problem in space and time [20, 57, 12]. While these approaches provide an elegant framework for joint segmentation and tracking, they are much more computationally intensive when compared to flow-based methods.

In most applications, cell segmentations are invaluable because it assists the user in subsequent downstream image analysis steps such as track validation and quantitative analysis (*e.g.* morphological features, image intensity). Thus, we propose a novel method with the following goals in mind:

- The segmentation instances should be computed jointly with tracking to avoid dependence on the accuracy of the segmentation method and to leverage both spatial and temporal information.
- The method should be computationally efficient and support out-of-memory processing of multi-terabyte datasets.
- It should leverage existing pre-trained models or traditional image processing for segmentation while achieving reasonable performance when ground-truth

labels are unavailable.

To accomplish this, we propose a new algorithm for joint segmentation and tracking. It builds upon the concept of hierarchical segmentation and a novel method for extracting disjoint segments from a hierarchy and, at the same time, formulating it as an integer linear program (ILP) that respects the biological constraints (*e.g.*, cell divides into two).

We perform multiple experiments evaluating different use cases of the proposed method and validate its performance against state-the-art-methods using the cell tracking challenge benchmark [60]. Moreover, we show our method can scale to large multi-terabyte scale real-world microscopy datasets [64] with millions of cell instances.

2 Background and Related Works

2.1 Hierarchical Segmentation

Hierarchical segmentation has previously been used in cell tracking [59] but in a very limited scenario. Here we review a more general representation of hierarchies and contours and their application to image segmentation.

Flat image segmentation (*i.e.* non-hierarchical) concerns partitioning an image into disjoint segments, while hierarchical segmentation produces nested regions. Let V be our basic units, the image voxels, a hierarchy $\mathcal{H} = \{S_1, S_2, \dots, S_n\}$ contains a sequence of segmentations, where every S_i is a collection of disjoint non-empty sets and their union is V . The sequence is ordered, such that S_{i-1} is a refinement of S_i , so any element in S_{i-1} is a subset of an individual region of S_i . Therefore, at the finest level, S_1 , each region contains a single unit, and at the coarsest, there is a single region $S_n = \{V\}$, the whole image. By assigning an increasing value λ_i for each partition S_i , the hierarchy can be represented as a dendrogram.

The hierarchical segmentation cannot be easily represented with a set of discrete labels as done for flat segmentation. Instead, they are commonly represented using an Ultrametric Contour Maps (UCM) [36, 34, 3] where the boundary between different regions receives the value λ_i of where their merging happened.

Several methodologies explore this duality between fuzzy contour maps (*i.e.* UCM, edge detection, affinity map) and hierarchies. Notably, Pont-Tuset *et al.* [48] accelerate the computation of the normalized cut [53] of image affinity maps by starting the clustering from a lower-resolution image and increasing its resolution, and finally aligning and merging the results into a UCM. Maninis *et al.* [29] used a convolutional neural network (CNN) to estimate boundaries of different orientations and applied the oriented watershed transform [4] to obtain the hierarchical segmentation.

In the more general context, these nested segmentations

are a hierarchical clustering of an edge-weighted graph $G = (V, E)$, where V are the image pixels and E the edges connecting nearby elements in the image planar lattice. For example, the watershed framework from [36] was extended to edge-weighted *image graphs* [8, 34].

In the microscopy domain, segmentation from edge weights is extremely popular [7, 13]. Because most applications expect a single label per instance, methodologies based on correlation clustering [21, 23, 65, 42] are preferred over hierarchical [40] because they avoid the extremely challenging step of selecting the segment from the hierarchy without using a naive horizontal cut in the dendrogram. Kiran and Serra [24] proposed an algorithm that finds the optimum flat partition in a hierarchy for a restricted set of energies. More recently, GASP [5] was proposed to unite correlation and hierarchical clustering.

Our approach is not constrained to any hierarchical segmentation method; we chose the watershed framework due to its simplicity and computational performance.

2.2 Cell Tracking

Cell tracking has been a central problem for the bioimage community for more than two decades [67]. Several different strategies have been explored, a non-exhaustive list being: contour evolution [10]; sequential fitting of Gaussian mixtures [2]; dynamics programming using the Viterbi algorithm [27]; and probabilistic graphical models that account for under/over-segmentation errors [51].

Most related to our approach are joint segmentation and tracking methods, where the final cell segments are found during the tracking step. In [59], the authors first compute a hierarchical segmentation by fitting ellipsoids to their cells detection binary map contours; next, they estimate their association score using gradient boosting [11]; and obtain the tracks by solving a network flow ILP.

Jug *et al.* [20] proposed (and later improved [49]) the moral lineage tracing problem by formulating tracking as a minimum cost multi-cut given the biological constraints, that cells can divide but not merge, and that they can appear or disappear from the field of view. This approach extended the wide literature of multi-cut problems in the spatial domain (*i.e.*, image segmentation) [21, 23, 65, 42] to include the time axis and additional constraints. Despite the elegant framework, the NP-hardness of the multi-cut problem limits its application to medium size datasets, even with specialized algorithms [49].

More recently, flow-based methods [16, 38, 56] were proposed and have shown the most competitive performance. In [17], they estimate both the centroid detection and the motions of cells using a CNN. The tracking is computed by advecting backward in time using motion estimation and starting from the cells' detections. Malin-Mayor *et al.* [28, 18] extends this method by proposing a loss function

that allows sparse annotation of the cells' centroids and their links, additionally, the lineages are obtained with an ILP solver rather than a heuristic as in earlier work [16, 17, 56].

Other notable DL-learning-based tracking methods employ different strategies: [44] tracks cells by clustering pixels from adjacent frames using their coordinates and embeddings from a recurrent hourglass network; Starting from a set of segments, Ben *et al.* [6] construct a directed graph and solves the tracking using a graph neural network to classify the edges that belong to the cell lineages.

3 Method

Our method was developed for fluorescence microscopy images, where cells are engineered to express nuclei-localized fluorescence labels making them easily identifiable from the background. The challenge is to split the cells' instances, which cannot be easily resolved because of optical blur, and link these instances through time.

To avoid committing to a single potentially erroneous candidate segment per cell, we construct a hierarchy of segments. Ideally, the true cell instance will be one of these candidate segments. This differs from methods that aggregate superpixels during tracking [20, 49] because the set of possible segments is fixed during the ILP optimization.

While it is rather optimistic to assume that the hierarchy will always closely fit the true segments, this approach can always find a single region at a finer level that belongs to a unique true segment at the cost of not covering it completely.

We formulate the problem of finding the instances in the hierarchy as an optimization problem to maximize the overlap between the *unknown* true instances and a selection of disjoint segments from the hierarchy, which we will call maximum total intersection over union (MTIoU).

Given a hierarchy \mathcal{H} and a set of ground-truth segments $\mathcal{G} = \{g_1, g_2, \dots, g_n\}$, the set of disjoint segmentation with MTIoU can be found with the following ILP:

$$\arg \max_{\mathbf{x}} = \sum_{p \in \mathcal{H}} \sum_{q \in \mathcal{G}} w_{pq} x_{pq} \quad (1)$$

$$\text{s.t. } y_p = \sum_{q \in \mathcal{G}} x_{pq} \quad \forall p \in \mathcal{H} \quad (2)$$

$$\sum_{p \in \mathcal{H}} x_{pq} \leq 1 \quad \forall q \in \mathcal{G} \quad (3)$$

$$y_p + y_q \leq 1 \quad \forall p, q \in \mathcal{H} | p \subset q \quad (4)$$

$$y_p \in \{0, 1\} \quad \forall p \in \mathcal{H} \quad (5)$$

$$x_{pq} \in \{0, 1\} \quad \forall p, q \in \mathcal{H} \times \mathcal{G} \quad (6)$$

where w_{pq} is the intersection over union (IoU) between segment p and q ; x_{pq} indicates if p is assigned to q ; y_p indicates if segment p was selected ($y_p = 1$) with Eq. 2 forcing

a single assignment per segment; Eq. 3 forces a single assignment per ground-truth segment; Eq. 4 restricts the solution to only disjoint segments (*i.e.* they belong to different branches of the hierarchy).

In practice, information about the true instances is not available, so we approximate this problem by solving the segmentation selection between hierarchies of adjacent frames under the assumption that they are similar. Thus, the cell segments will overlap in some nodes in the hierarchies.

By formulating the ILP considering every time point, not just a pair of frames, and including the biological constraints, such as cell division, disappearing and appearing cells [59], the resulting segmentation and their association between hierarchies can reconstruct the cell lineages.

Therefore, the ILP formulation of the MTIoU between hierarchies for cell tracking becomes:

$$\arg \max_{\mathbf{x}} = \sum_{t \in [2..T-1]} \sum_{p \in \mathcal{H}_{t-1}} \sum_{q \in \mathcal{H}_t} w_{pq} x_{pq} + \sum_{p \in \mathcal{H}} w_{\alpha} x_{\alpha p} + w_{\beta} x_{p\beta} + w_{\delta} x_{\delta p} \quad (7)$$

$$\text{s.t. } y_q = x_{\alpha q} + \sum_{p \in \mathcal{H}_{t-1}} x_{pq} \quad \forall q \in \mathcal{H}_t \quad \forall t \in [1..T] \quad (8)$$

$$y_p + x_{\delta p} = x_{p\beta} + \sum_{q \in \mathcal{H}_{t+1}} x_{pq} \quad \forall p \in \mathcal{H}_t \quad \forall t \in [1..T] \quad (9)$$

$$y_p \geq x_{\delta p} \quad \forall p \in \mathcal{H} \quad (10)$$

$$y_p + y_q \leq 1 \quad \forall p, q \in \mathcal{H}_t | p \subset q \quad \forall t \in [1..T] \quad (11)$$

$$y_p \in \{0, 1\} \quad \forall p \in \mathcal{H} \quad (12)$$

$$x_{pq} \in \{0, 1\} \quad \forall p, q \in \mathcal{H}_{t-1} \times \mathcal{H}_t \quad \forall t \in [2..T] \quad (13)$$

where \mathcal{H}_t is the candidate segments (*i.e.* hierarchy) of frame t and $\mathcal{H} = \cup_{t \in [1..T]} \mathcal{H}_t$. We consider $\mathcal{H}_t = \emptyset$ when t is out of range $[1..T]$; $x_{\alpha p}, x_{p\beta}, x_{\delta p}$ are the segment p appearance, disappearance, and division binary variables, respectively; $w_{\alpha}, w_{\beta}, w_{\delta}$ their non-positive-valued penalization parameters, the starting and ending frames are not penalized, so $w_{\alpha} = 0$ for segments from $t = 1$ and $w_{\beta} = 0$ from $t = T$; y_p is a slack binary variable indicating if segment i is part of the solution. Equation 8 and 9 are the constant flow constraints [59] such that for the selected segments, there is an incoming segment from the previous frame or it is an appearing segment, and the outflow allows up to 2 out-going segments (*i.e.* division) or its disappearance; Eq. 10 asserts there are only divisions from an existing cell; Eq. 11 restricts the solution to disjoint segments as in Eq. 4. In Section 4.3, we compare the run time of our ILP formulation with previous work.

Note that due to the additive nature of the MTIoU objective function, it can lead to over-segmentation. Two simple strategies to circumvent this are proposed in Section 3.2.

3.1 Hierarchy construction

The hierarchies are computed using the hierarchical watershed framework [47, 45], which allows constructing hierarchies in log-linear time (sorting complexity) with respect to the number of edges in a graph with the minimum-spanning tree algorithm [35] and Tarjan union-find [58].

For each frame t , we estimate a set of candidate segments, \mathcal{H}_t , from a binary detection, D_t , and a fuzzy contour map, C_t , provided by the user. The detection D_t indicates the location of cells and background. The contour map indicates where the cell boundaries (*i.e.* contours) may lie. Since the connected components in D_t are disconnected by definition, a hierarchy is computed for each one and integrated into a single \mathcal{H}_t while ignoring the background.

Each hierarchy is constructed using the watershed hierarchy by area [32, 45] on the undirected weighted graph from their respective connected component in D_t . The edge weight between a pair of pixels is their average intensity.

Using the full hierarchies on the tracking ILP (Eq. 7) can easily make the problem too large to solve. Therefore, three criteria were used to filter irrelevant segments [46] and decrease the number of candidate solutions:

1. Minimum size: the hierarchy is pruned below a minimum size threshold;
2. Maximum size: the hierarchy is cut above a maximum size threshold;
3. Non-relevant contours: segments with average contour strength below a threshold are fused.

The minimum and maximum cell sizes are usually known for each organism, and the non-relevant contours filtering can be tuned by observing the under (over) segmentation of the solution. Figure 1 shows a hierarchy filtering example.

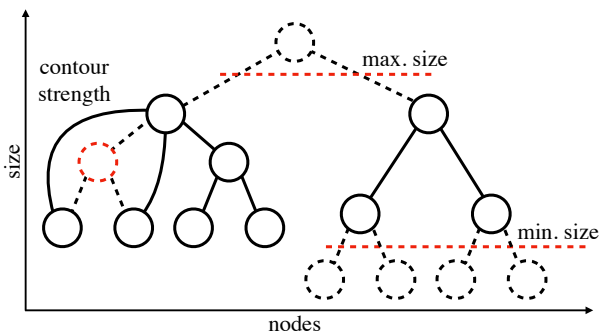


Figure 1: Example of hierarchy filtering by minimum size, maximum size, and contour strength; dashed lines show deleted elements. Leaves of the hierarchy are not shown.

3.2 Avoiding over segmentation

Despite the segment filtering described in the previous Section, the MTIoU can suffer from over-segmentation when

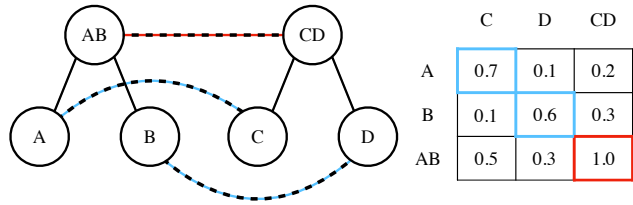


Figure 2: Example of linkage between two hierarchies and their weights matrix $w_{..}$ which includes all $w_{p,q}$. Solution considering $w_{..}$ in blue and in red solution of $w_{..}^p$ when $p \geq 2$.

spurious segments with high overlap between frames are present in the hierarchies.

For example, in Figure 2, despite AB and CD having perfect overlap ($w_{AB,CD} = 1.0$) when solving Eq. 7, the solution selects segments A, B, C, D (blue solution) because their sum of weights is larger. By taking a power p of $w_{..}$, we reduce the over-segmentation as it favors fewer segments with larger $w_{..}$ values (red solution) rather than many with smaller $w_{..}$ values. However, this does not improve the segmentation when the spurious segments have large $w_{..}$, and we notice this phenomenon happens even when joint tracking and segmentation appear trivial.

When the spurious segments have large $w_{..}$, noise can improve the segmentation. Assume we have two identical frames with two cells, Figure 3a (single frame shown), where the segmentation would be trivial. The MTIoU between these frames will yield the solution with the most segments because each region in the hierarchy will have perfect overlap with its sibling region from the adjacent frame because they are identical. Therefore, only when filtering the hierarchy perfectly will it yield the correct segmentation, which is challenging to do in practice. Figures 3e and 3f show the results for two commonly used contour topologies, the complement of a distance transform (Fig. 3b), and a binary contour (Fig. 3c). In every scenario, the hierarchies were pruned by removing regions smaller than 7 pixels.

The arbitrary partitions in Figures 3e, 3f and UCM representation (3d) are a result of tie-zones, where the watershed solution is non-unique. Different implementations have their own tie-breaking policies, these policies are often consistent, and similar patterns occur for similar adjacent frames, causing the selection of spurious segments.

By perturbing the contour topologies with random noise, we disrupt the overlap of regions where there is no true contour, resulting in the expected segmentation results, Figures 3h and 3i, for their respective contours, Figures 3b and 3c.

The perturbed hierarchies are created by adding a positive noise to the input contour map (Fig. 3b and 3c). This improves the contrast between the weights $w_{..}$ of the true segments and the spurious ones by decreasing the IoU be-

tween regions that are not robust to perturbations. This is valid as long as the noise is lower than the estimated contours of the true segments and the noise is positive — negative noise can lead to leaks in the watershed operator. This simple solution was crucial to obtain the top score for some datasets (see supplementary for comparison).

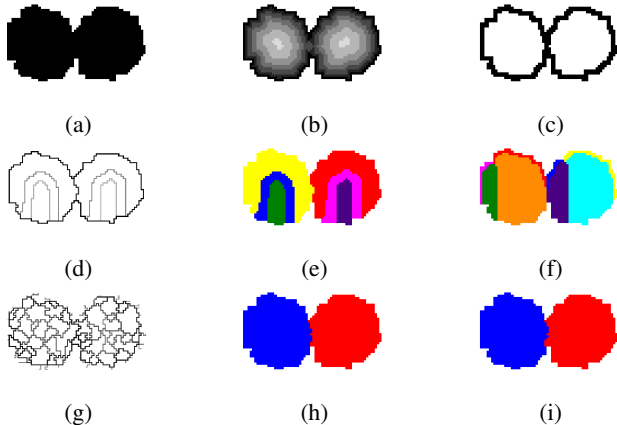


Figure 3: Comparison between segmentation results from maximum total intersection over union (MTIoU) between two hierarchies from the same input with and without perturbation (a) Input mask; (b) complement of distance transform (CDT); (c) Binary Contour; (d) ultrametric contour map (UCM) from CDT; (e) MTIoU segmentation from CDT; (f) MTIoU from binary contour; (g) UCM from perturbed CDT; (h) perturbed MTIoU segmentation from CDT; (i) perturbed MTIoU segmentation from the binary contour.

3.3 Scaling to terabyte-scale datasets

As described previously, one major limitation of joint segmentation and tracking is the intense computational requirements. In this section, we describe the strategies for scaling our method to terabyte-scale datasets.

The hierarchical segmentation is computed per connected component of each detection map D_t , greatly reducing the number of pixels considered. For each hierarchy, the segments outside of the minimum and maximum size range are removed. Next, the disjoint segmentation constraint, Eq. 11, is computed by going through each segment to its last ancestor. For each segment, we store their center coordinates and bounding boxes for computing their IoU. Since the segmentation of each volume (plane) is independent, it can be easily run in parallel.

The association weight between segments is only computed for a subset of $k \times N_t$ pairs, where N_t is the total number of segments on frame t . For $(t - 1, t)$ -pair of frames, we start by computing a KDTree [62] with the segments' coordinates from $t - 1$ and querying the $2k$ -nearest neighbors within a certain radius for each segment coordinate in

t . From these $2k$ samples, we select the k with the highest IoU, thus, we avoid computing the $w_{..}$ for every pair in $(t - 1, t)$, as $w_{..}$ is significantly sparse. Additionally, since the IoU only considers the positive values of the segmentation masks, it can be computed using a crop around the segments' bounding box. When the bounding boxes between a segment and its neighbor do not intersect, its IoU is zero and does not require further computation. The weights between different $(t - 1, t)$ are independent, so each pair of frames can be run in parallel.

The ILP can easily reach millions of variables due to multiple candidate segments per cell. When that happens, it cannot be solved in a reasonable amount of memory or time. However, its global solution can be approximated by solving the problem in multiple overlapping time windows as in [28]. The regions between overlapping windows are not used in the final solution because they can be of lower quality for being near the windows' boundaries. The segments already present in the global solution are added as constraints to stitch tracks between windows.

Malin-Mayor *et al.* [28] employed their own distributed computing scheduler to process these windows in parallel while avoiding concurrent processing of overlapping windows. We propose a simpler two-pass interleaved scheduling scheme: i) Split the time lapse only along the time-axis into N overlapping windows, where the overlap is smaller than a single window; ii) Solve the ILPs of the even-numbered window; iii) Add the solutions from the even-numbered ILPs as constraints; and iv) solve the odd-numbered ILPs. This simple strategy guarantees that no overlapping window is processed at the same time, and it can be trivially executed in parallel at the cost of waiting for every even-numbered window to finish before starting the odd-numbered executions. Further improvements can be made by waiting for only adjacent pairs to finish (*e.g.* window 3 depends on 2 and 4).

4 Experiments

We evaluate our claims and the proposed method in four different experiments:

1. Analysis of an ensemble of segmentations with traditional segmentation algorithms and off-the-shelf segmentation CNNs.
2. Quantitative comparison of the proposed algorithm against state-of-the-art methods for cell tracking.
3. Run time comparison of different ILP formulations.
4. Qualitative comparison of our algorithm in a multi-terabyte dataset.

The first experiment runs on the training set of Fluo-N2DL-HeLa [37], a 2D dataset of HeLa cells expressing H2b-GFP from the cell-tracking challenge (CTC) [60], we chose this dataset since it contains high-quality images and

annotations. As this dataset is 2D, we can leverage state-of-the-art off-the-shelf 2D segmentation methods such as Cellpose [55] and Stardist [52].

The quantitative experiment was evaluated using the metrics proposed by CTC: TRA, a score of operations required to transform the resulting lineage graph to the ground-truth lineage [30]; SEG, the average IoU between the predicted and the ground-truth segmentation instances (a predicted instance is assigned to a ground-truth instance when it overlaps with more than half of its pixels); and CTB, the average between the TRA and SEG scores, it is the main ranking score in the competition.

For our implementation, we used Gurobi [14] to solve the ILP. The deep learning routines used PyTorch [43]. The hierarchical segmentation was done using Higr [45]. Throughout the code, we heavily used NumPy [15], SciPy [62], CuPy [39] and scikit-image [61].

4.1 Segmentation ensemble experiment

Most biologists cannot train their own segmentation models or design complex image-processing pipelines. Therefore, leveraging broadly available segmentation tools is important. We show that our method can use segmentations from different algorithms and combine them to achieve superior performance using fuzzy contour map representations.

We evaluate three different segmentation methods: a classical watershed from h-minima using a distance transform as the watershed basins [25, 61]; Cellpose [55] using their nuclei pre-trained model; and Stardist [52] using their "2d versatile fluorescence" pre-trained model.

For each segmentation map, we extract a binary map indicating foreground (*i.e.* cell) versus background and the distinct labels' binary contours. The ensemble maps were created by combining the detections using the logical OR operator and the contours by averaging. Table 1 presents the tracking and segmentation scores from running our proposed algorithm on the foreground and contour maps from the labels of each method. The top score for the ensemble model shows that the contour map representation is an effective way to combine multiple segmentations and consequently improve cell tracking. Figure 4 shows an example where this approach benefits segmentation and tracking.

4.2 Quantitative comparison

The second experiment is run on four datasets from CTC: Fluo-C3DL-MDA231: Infected human breast carcinoma cells; Fluo-N3DH-CE: *C. Elegans* developing embryo [33]; Fluo-N3DL-DRO: *D. Melanogaster* developing embryo [2]; Fluo-N3DL-TRIC: Cartographic projection of developing *Tribolium Castaneum* embryo. In each case, two sets of images are available for training and validation purposes, and two other images are used for testing. Test set results were

File	Method	TRA	SEG	CTB
1	Watershed	0.905	0.593	0.749
	Cellpose	0.863	0.671	0.767
	Stardist	0.910	0.724	0.817
	Ensemble	0.956	0.740	0.848
2	Watershed	0.898	0.695	0.796
	Cellpose	0.908	0.743	0.825
	Stardist	0.941	0.818	0.880
	Ensemble	0.956	0.826	0.891

Table 1: Tracking and segmentation results for individual segmentation methods and their ensemble.

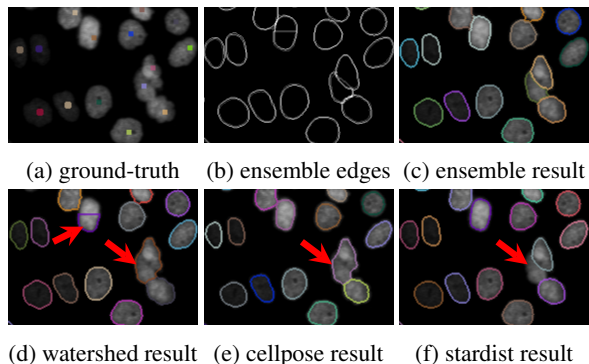


Figure 4: Results from individual methods versus their ensemble, mistakes are indicated by the red arrows. (a) ground-truth cell detection; (e) ensemble edge map; and (c) result; (d-f) segmentation results of different methods.

evaluated by the competition organizers and their labels are not publicly available.

The MDA231 and CE datasets have ground-truth tracks and silver-standard segmentation annotation automatically generated by a consensus [1] of the top-ranking algorithms from previous iterations of CTC. The DRO and TRIC datasets only have ground-truth tracks for a specific group of cells and a few 2D labels. The initial positions of these cells' tracks are provided during submission and used to filter the lineages. These sparse annotations make the tracking much more challenging because less training data are available, and other lineages must be removed, so missing links on the predicted lineages will prune the rest of the lineage and greatly decrease the final score.

Before processing, all images were linearly interpolated to make them isotropic and normalized using their quantiles. While isotropy is not necessary, it benefits the algorithm's accuracy.

We used a U-Net CNN [50] for predicting the cell and edge detection maps, and both maps were optimized using their own dice loss [9] with additional dice losses on side

edge-detection predictions [63] during training.

The DRO and TRIC do not have any 3D segmentation annotations. Therefore, we tried two approaches. i) Using our U-Net and training it using labels computed from a traditional segmentation algorithm. We denoted this as pseudo-labels (PL). ii) And using image processing operators to detect the cells and compute the contour topology, denoted by image processing (IM).

In both cases, the cells were detected using a difference of Gaussians and thresholding it with Otsu. The contour maps were simply the inverse of the Gaussian blurred image. For the pseudo-labels, we used the contour maps and detections to run the hierarchical watershed and performed a horizontal cut in the hierarchy to obtain the flat segments used for training our CNN. In IM, they were used as the tracking input.

We optimized the hyper-parameters using grid search and cross-validation on the training set to avoid a biased estimate of our final accuracy, so models trained on dataset 01 were applied to dataset 02 and the other way around. More details about these procedures, including their parameters, can be found in the supplementary materials.

The image-processing solutions achieved better results (see supplementary) on these two datasets than deep learning combined with pseudo-labels, therefore, IM was used in our final submission. Next, the proposed method was evaluated on the hidden test set.

The competition organizers report the top three methods for each metric and provide access to our ranking regardless of our position. The final results are reported in Table 2.

The top-scoring methods at the time of submission were:

1. KTH-SE: [27] image processing solution with tracking using Viterbi algorithm;
2. KIT-GE: EmbedTrack [26], a joint flow-based tracking and pixel embedding segmentation method;
3. MPI-GE-CBG: Description is not publicly available, source code indicates it is a DL flow-based method with advection nearest neighbor linking;
4. JAN-US: [18] it is an improved version of [28], where they classify the cell states to detect division and assist the ILP formulation and use a structured SVM to find the optimal weights of the ILP automatically;
5. LEID-NL: Model-evolution method [10] with additional routines to split dividing cells and track cells entering the field of view;
6. MU-CZ: H-minima watershed [31] plus U-Net for cell contour and detection prediction, tracking uses an intersection-based heuristic;
7. IGFL-FR: ELEPHANT [56] uses the cell detection and advection of DL flow prediction linking as MPI-GE-CBG method.

Our approach obtained the best performance in the combined score, CTB, on two out of the four datasets, one being the CE with supervised DL and the DRO with image

Dataset	Rank	TRA	SEG	CTB
MDA231	1st	0.884 ²	0.710 ²	0.797 ²
	2nd	0.882 ¹	0.642 ⁵	0.761 ⁵
	3rd	0.880 ⁵	0.632 ¹	0.757 ¹
	7th	0.818	0.549	0.683
CE	1st	0.987 ³	0.759 ⁶	0.844
	2nd	0.979 ⁴	0.729 ²	0.829 ¹
	3rd	0.975 ⁷	0.722 ¹	0.808 ²
	4th	0.967	0.722	-
DRO	1st	0.805	0.567 ¹	0.661
	2nd	0.785 ⁴	0.518	0.617 ¹
	3rd	0.785 ³	0.397 ⁴	0.591 ⁴
TRIC	1st	0.952 ³	0.791 ¹	0.867 ¹
	2nd	0.942 ¹	0.766 ²	0.816 ³
	3rd	0.898	0.680 ³	0.787 ²
	4th	-	0.666	0.782

Table 2: Results on the hidden test dataset of the cell tracking challenge at the time of article submission; subscripts indicate the method used according to enumeration; our submission is in bold (anonymous submission on the competition website until paper acceptance).

processing only. In the TRIC dataset, most of our mistakes were on the periphery of the projection, where the cells’ movements are inflated, resulting in little overlap, making our IoU weights significantly less effective. In the MDA231 we achieved our worst ranking, we suspect our hyper-parameter estimation did not generalize to the test dataset.

4.3 ILP run time comparison

Cells moving in and out of the field of view and cell division constraints are critical aspects of the cell-tracking ILP and can be formulated in different ways. In this experiment, we compare the performance of our formula against other recent ILP-based methods for optimizing Eq. 7, Türetken *et al.* [59] and Malin-Mayor *et al.* [28], with the same experimental setup and parameters. We included Eq. 11 to Malin-Mayor formulation to allow multiple segmentation hypotheses and set $w_\beta = 0$ for all methods because Malin-Mayor does not penalize disappearance events.

We compared the average run time of 3 runs with an increasingly wide time window of the Fluo-N3DH-CE datasets. The windows started from the middle of the time-lapse and increased at both ends. A linear fit for each group reported slope coefficients of 1.75 ± 0.12 for Türetken, 1.37 ± 0.06 for Ours, and 1.84 ± 0.06 for Malin-Mayor, the smaller, the better. Figure 5 display the measurements and their linear regression. Therefore, our formulation is

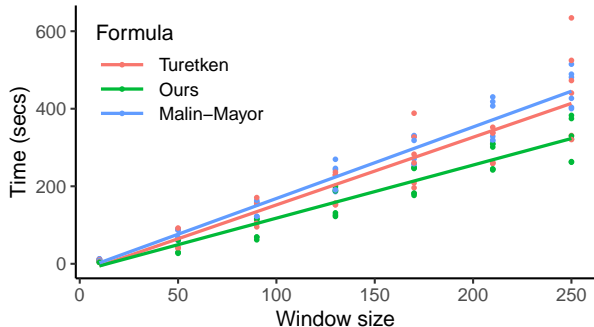


Figure 5: Run time comparison between different ILP formulations.

faster and scales better with increasingly larger problems.

4.4 Large dataset qualitative comparison

We ran our algorithm on a 3D time-lapse dataset of a developing zebrafish embryo [64] recorded with a light-sheet microscope. The recording starts at 12 hrs post fertilization and lasts 6.6 hrs with an acquisition interval of 30 secs. After cropping and stabilizing the region containing the embryo, the dataset’s uncompressed size is about 3.4 TB, and its shape is $791 \times 448 \times 2174 \times 2423$ voxels (t, z, y, x).

The algorithm was executed in a compute cluster using SLURM [66], following the strategies described in Section 3.3. For the tracking step, a window of size 50 with an overlap of 5 frames on each side was used. For a fair comparison, we limited our resources to 100 CPU cores and 20 GPUs as used in [28].

Processing took approximately a total of 9.5 hours of distributed computing, including: 1 hour and 20 min. to detect and predict the contours using a U-Net as described in the other experiments, and trained on pseudo-labels from a watershed segmentation; 2 hours and 7 min. to compute the hierarchical segmentation for all frames; 40 minutes for the association between segments; 3 hours for the tracking first pass; 2 hours and 8 minutes for the second pass; and 18 minutes to export the data. The first step used GPUs, the remaining only CPU cores, processing in total 1 day 1 hour of GPU time, and 31 days 22 hours of CPU time. Resulting in more than 21.5 million cell instances. The ILP size is partially proportional to the number of resulting instances.

In comparison, with similar resources, Malin-Mayor *et al.* [28] tracked a mouse dataset in an earlier developmental stage (therefore, fewer and less densely distributed nuclei) in 44 hours, segmenting about 7 million cell instances. Information about the total GPU and CPU time is not available. Figure 6 shows our method segmentation results.

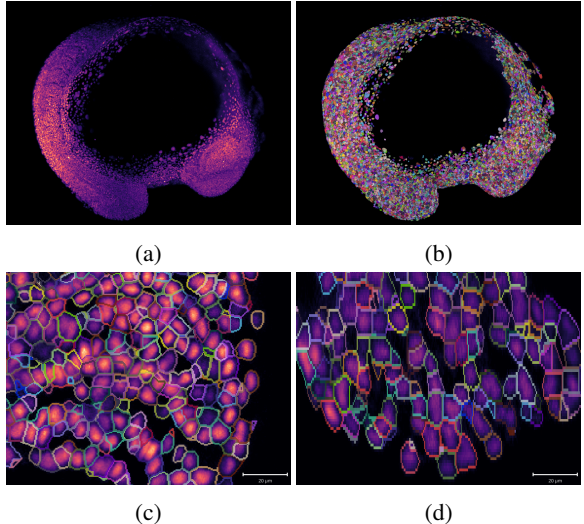


Figure 6: Whole embryo segmentation results: (a) Maximum intensity projection; (b) 3D rendering of segmentation labels; (c) YX slice; and (d) ZY slice.

5 Conclusion

In this paper, we introduced a novel approach to cell tracking in microscopy data that selects cell segments from hierarchical segmentations. Our method demonstrated superior performance on two out of four datasets from the cell tracking challenge [60] and was able to scale to terabyte-scale datasets. However, the benefits of using contour maps for cell tracking extend beyond surpassing benchmark metrics and improving segmentation performance. The contour (*i.e.* affinity) space offers more flexibility than the traditional domain of discrete labels, enabling the use of an ensemble of segmentation models and differential models for edge detection. As future work, our method can be adapted to leverage motion information from flow-based methods, providing a more robust and powerful approach than the commonly used non-maximum suppression for filtering out cell detections. Overall, we believe our approach has significant potential for advancing cell tracking in complex microscopy data and opening new avenues for exploration in bioimaging research.

Acknowledgements

We thank Ahmet Can Solak, Alexandre Falcão, Guillaume Le Treut, Laurent Najman, and Sandy Schmid for proof-reading and giving feedback on our manuscript and Chan Zuckerberg Biohub for supporting this work.

References

- [1] Cem Emre Akbaş, Vladimír Ulman, Martin Maška, Florian Jug, and Michal Kozubek. Automatic fusion of segmentation and tracking labels. In *Computer Vision—ECCV 2018 Workshops: Munich, Germany, September 8–14, 2018, Proceedings, Part VI 15*, pages 446–454. Springer, 2019. [6](#)
- [2] Fernando Amat, William Lemon, Daniel P Mossing, Katie McDole, Yinan Wan, Kristin Branson, Eugene W Myers, and Philipp J Keller. Fast, accurate reconstruction of cell lineages from large-scale fluorescence microscopy data. *Nature Methods*, 11(9):951–958, 2014. [1](#), [2](#), [6](#)
- [3] Pablo Arbelaez. Boundary extraction in natural images using ultrametric contour maps. In *Conference on Computer Vision and Pattern Recognition Workshop*, pages 182–182. IEEE, 2006. [2](#)
- [4] Pablo Arbelaez, Michael Maire, Charless Fowlkes, and Jitendra Malik. Contour detection and hierarchical image segmentation. *IEEE Transactions on Pattern Analysis and Machine Intelligence*, 33(5):898–916, 2010. [2](#)
- [5] Alberto Bailoni, Constantin Pape, Nathan Hütsch, Steffen Wolf, Thorsten Beier, Anna Kreshuk, and Fred A Hamprecht. GASP, a generalized framework for agglomerative clustering of signed graphs and its application to instance segmentation. In *IEEE Conference on Computer Vision and Pattern Recognition*, pages 11645–11655, 2022. [2](#)
- [6] Tal Ben-Haim and Tammy Riklin Raviv. Graph neural network for cell tracking in microscopy videos. In *European Conference on Computer Vision*, pages 610–626. Springer, 2022. [3](#)
- [7] Kevin Briggman, Winfried Denk, Sebastian Seung, Moritz Helmstaedter, and Srinivas C Turaga. Maximin affinity learning of image segmentation. volume 22, 2009. [2](#)
- [8] Jean Cousty, Gilles Bertrand, Laurent Najman, and Michel Couprie. Watershed cuts: Minimum spanning forests and the drop of water principle. *IEEE Transactions on Pattern Analysis and Machine Intelligence*, 31(8):1362–1374, 2009. [2](#)
- [9] Ruoxi Deng, Chunhua Shen, Shengjun Liu, Huibing Wang, and Xinru Liu. Learning to predict crisp boundaries. In *European Conference on Computer Vision*, pages 562–578, 2018. [6](#)
- [10] Oleh Dzyubachyk, Wiggert A Van Cappellen, Jeroen Essers, Wiro J Niessen, and Erik Meijering. Advanced level-set-based cell tracking in time-lapse fluorescence microscopy. *IEEE Transactions on Medical Imaging*, 29(3):852–867, 2010. [2](#), [7](#)
- [11] Jerome H Friedman. Stochastic gradient boosting. *Computational statistics & data analysis*, 38(4):367–378, 2002. [2](#)
- [12] Jan Funke, Lisa Mais, Andrew Champion, Natalie Dye, and Dagmar Kainmueller. A benchmark for epithelial cell tracking. In *Proceedings of The European Conference on Computer Vision (ECCV) Workshops*, pages 0–0, 2018. [1](#)
- [13] Jan Funke, Fabian Tschopp, William Grisaitis, Arlo Sheridan, Chandan Singh, Stephan Saalfeld, and Srinivas C Turaga. Large scale image segmentation with structured loss based deep learning for connectome reconstruction. *IEEE Transactions on Pattern Analysis and Machine Intelligence*, 41(7):1669–1680, 2018. [2](#)
- [14] Gurobi Optimization, LLC. Gurobi Optimizer Reference Manual, 2023. [6](#)
- [15] Charles R Harris, K Jarrod Millman, Stéfan J van der Walt, Ralf Gommers, Pauli Virtanen, David Cournapeau, Eric Wieser, Julian Taylor, Sebastian Berg, Nathaniel J Smith, et al. Array programming with numpy. *Nature*, 585(7825):357–362, 2020. [6](#)
- [16] Junya Hayashida and Ryoma Bise. Cell tracking with deep learning for cell detection and motion estimation in low-frame-rate. In *International Conference on Medical Image Computing and Computer-Assisted Intervention*, pages 397–405. Springer, 2019. [1](#), [2](#), [3](#)
- [17] Junya Hayashida, Kazuya Nishimura, and Ryoma Bise. Mpm: Joint representation of motion and position map for cell tracking. In *IEEE Conference on Computer Vision and Pattern Recognition*, pages 3823–3832, 2020. [1](#), [2](#), [3](#)
- [18] Peter Hirsch, Caroline Malin-Mayor, Anthony Santella, Stephan Preibisch, Dagmar Kainmueller, and Jan Funke. Tracking by weakly-supervised learning and graph optimization for whole-embryo c. elegans lineages. In *International Conference on Medical Image Computing and Computer-Assisted Intervention*, pages 25–35. Springer, 2022. [1](#), [2](#), [7](#)
- [19] Jan Huiskens, Jim Swoger, Filippo Del Bene, Joachim Wittbrodt, and Ernst HK Stelzer. Optical sectioning deep inside live embryos by selective plane illumination microscopy. *Science*, 305(5686):1007–1009, 2004. [1](#)
- [20] Florian Jug, Evgeny Levinkov, Corinna Blasse, Eugene W Myers, and Bjoern Andres. Moral lineage tracing. In *IEEE Conference on Computer Vision and Pattern Recognition*, pages 5926–5935, 2016. [1](#), [2](#), [3](#)
- [21] Jörg Hendrik Kappes, Markus Speth, Björn Andres, Gerhard Reinelt, and Christoph Schn. Globally optimal image partitioning by multicuts. In *Energy Minimization Methods in Computer Vision and Pattern Recognition*, pages 31–44. Springer, 2011. [2](#)
- [22] Philipp J Keller, Annette D Schmidt, Joachim Wittbrodt, and Ernst HK Stelzer. Reconstruction of zebrafish early embryonic development by scanned light sheet microscopy. *Science*, 322(5904):1065–1069, 2008. [1](#)
- [23] Margret Keuper, Evgeny Levinkov, Nicolas Bonneel, Guillaume Lavoué, Thomas Brox, and Bjorn Andres. Efficient decomposition of image and mesh graphs by lifted multicuts. In *IEEE International Conference on Computer Vision*, pages 1751–1759, 2015. [2](#)
- [24] B Ravi Kiran and Jean Serra. Global–local optimizations by hierarchical cuts and climbing energies. *Pattern Recognition*, 47(1):12–24, 2014. [2](#)
- [25] Roberto de A Lotufo, Alexandre X Falcão, and Francisco A Zampiroli. IFT-watershed from gray-scale marker. In *Conf. on Graphics, Patterns and Images (SIBGRAPI)*, pages 146–152. IEEE, 2002. [6](#)
- [26] Katharina Löffler and Ralf Mikut. Embed-track—simultaneous cell segmentation and tracking through learning offsets and clustering bandwidths. *IEEE Access*, 10:77147–77157, 2022. [7](#)

- [27] Klas EG Magnusson. *Segmentation and tracking of cells and particles in time-lapse microscopy*. PhD thesis, KTH Royal Institute of Technology, 2016. 1, 2, 7
- [28] Caroline Malin-Mayor, Peter Hirsch, Leo Guignard, Katie McDole, Yanan Wan, William C Lemon, Dagmar Kainmueller, Philipp J Keller, Stephan Preibisch, and Jan Funke. Automated reconstruction of whole-embryo cell lineages by learning from sparse annotations. *Nature Biotechnology*, pages 1–6, 2022. 1, 2, 5, 7, 8
- [29] Kevis-Kokitsi Maninis, Jordi Pont-Tuset, Pablo Arbeláez, and Luc Van Gool. Convolutional oriented boundaries: From image segmentation to high-level tasks. *IEEE Transactions on Pattern Analysis and Machine Intelligence*, 40(4):819–833, 2017. 2
- [30] Pavel Matula, Martin Maška, Dmitry V Sorokin, Petr Matula, Carlos Ortiz-de Solórzano, and Michal Kozubek. Cell tracking accuracy measurement based on comparison of acyclic oriented graphs. *PLoS one*, 10(12):e0144959, 2015. 6
- [31] Fernand Meyer. Morphological segmentation revisited. *Space, Structure and Randomness: Contributions in Honor of Georges Matheron in the Field of Geostatistics, Random Sets and Mathematical Morphology*, pages 315–347, 2005. 7
- [32] Fernand Meyer, Albert Oliveras Vergés, Philippe Jean Salembier Clairon, and Corinne Vachier. Morphological tools for segmentation: connected operators and watersheds. *Annales des télécommunications. Annals of telecommunications*, 52(7-8):366–379, 1997. 4
- [33] John Isaac Murray, Zhirong Bao, Thomas J Boyle, Max E Boeck, Barbara L Mericle, Thomas J Nicholas, Zhongying Zhao, Matthew J Sandel, and Robert H Waterston. Automated analysis of embryonic gene expression with cellular resolution in *c. elegans*. *Nature Methods*, 5(8):703–709, 2008. 6
- [34] Laurent Najman. On the equivalence between hierarchical segmentations and ultrametric watersheds. *Journal of Mathematical Imaging and Vision*, 40(3):231–247, 2011. 2
- [35] Laurent Najman, Jean Cousty, and Benjamin Perret. Playing with kruskal: algorithms for morphological trees in edge-weighted graphs. In *Mathematical Morphology and Its Applications to Signal and Image Processing*, pages 135–146. Springer, 2013. 4
- [36] Laurent Najman and Michel Schmitt. Geodesic saliency of watershed contours and hierarchical segmentation. *IEEE Transactions on Pattern Analysis and Machine Intelligence*, 18(12):1163–1173, 1996. 2
- [37] Beate Neumann, Thomas Walter, Jean-Karim Hériché, Jutta Bulkescher, Holger Erfle, Christian Conrad, Phill Rogers, Ina Poser, Michael Held, Urban Liebel, et al. Phenotypic profiling of the human genome by time-lapse microscopy reveals cell division genes. *Nature*, 464(7289):721–727, 2010. 5
- [38] Kazuya Nishimura, Junya Hayashida, Chenyang Wang, Dai Fei Elmer Ker, and Ryoma Bise. Weakly-supervised cell tracking via backward-and-forward propagation. In *European Conference on Computer Vision*, pages 104–121. Springer, 2020. 2
- [39] Royud Nishino and Shohei Hido Crissman Loomis. Cupy: A numpy-compatible library for nvidia GPU calculations. *Advances in Neural Information Processing Systems Workshop*, 151(7), 2017. 6
- [40] Juan Nunez-Iglesias, Ryan Kennedy, Toufiq Parag, Jianbo Shi, and Dmitri B Chklovskii. Machine learning of hierarchical clustering to segment 2d and 3d images. *PLoS one*, 8(8):e71715, 2013. 2
- [41] Wei Ouyang, Fynn Beuttenmueller, Estibaliz Gómez-de Mariscal, Constantin Pape, Tom Burke, Carlos Garcia-López-de Haro, Craig Russell, Lucía Moya-Sans, Cristina de-la Torre-Gutiérrez, Deborah Schmidt, et al. Bioimage model zoo: A community-driven resource for accessible deep learning in bioimage analysis. *bioRxiv*, 2022. 1
- [42] Constantin Pape, Thorsten Beier, Peter Li, Viren Jain, Davi D Bock, and Anna Kreshuk. Solving large multicut problems for connectomics via domain decomposition. In *Proceedings of the IEEE International conference on computer vision workshops*, pages 1–10, 2017. 2
- [43] Adam Paszke, Sam Gross, Francisco Massa, Adam Lerer, James Bradbury, Gregory Chanan, Trevor Killeen, Zeming Lin, Natalia Gimelshein, Luca Antiga, et al. Pytorch: An imperative style, high-performance deep learning library. In *Advances in Neural Information Processing Systems*, pages 8026–8037, 2019. 6
- [44] Christian Payer, Darko Štern, Thomas Neff, Horst Bischof, and Martin Urschler. Instance segmentation and tracking with cosine embeddings and recurrent hourglass networks. In *International Conference on Medical Image Computing and Computer-Assisted Intervention*, pages 3–11. Springer, 2018. 3
- [45] Benjamin Perret, Giovanni Chierchia, Jean Cousty, Silvio Jamil Ferzoli Guimaraes, Yukiko Kenmochi, and Laurent Najman. Higr: Hierarchical graph analysis. *SoftwareX*, 10:100335, 2019. 4, 6
- [46] Benjamin Perret, Jean Cousty, Silvio Jamil Ferzoli Guimaraes, Yukiko Kenmochi, and Laurent Najman. Removing non-significant regions in hierarchical clustering and segmentation. *Pattern Recognition Letters*, 128:433–439, 2019. 4
- [47] Benjamin Perret, Jean Cousty, Silvio Jamil F Guimaraes, and Deise S Maia. Evaluation of hierarchical watersheds. *IEEE Transactions on Image Processing*, 27(4):1676–1688, 2017. 4
- [48] Jordi Pont-Tuset, Pablo Arbeláez, Jonathan T Barron, Ferran Marques, and Jitendra Malik. Multiscale combinatorial grouping for image segmentation and object proposal generation. *IEEE Transactions on Pattern Analysis and Machine Intelligence*, 39(1):128–140, 2016. 2
- [49] Markus Rempfler, Jan-Hendrik Lange, Florian Jug, Corinna Blasse, Eugene W Myers, Bjoern H Menze, and Bjoern Andres. Efficient algorithms for moral lineage tracing. In *IEEE International Conference on Computer Vision*, pages 4695–4704, 2017. 2, 3
- [50] Olaf Ronneberger, Philipp Fischer, and Thomas Brox. U-net: Convolutional networks for biomedical image segmentation. In *International Conference on Medical image com-*

- puting and computer-assisted intervention, pages 234–241. Springer, 2015. 6
- [51] Martin Schiegg, Philipp Hanslovsky, Bernhard X Kausler, Lars Hufnagel, and Fred A Hamprecht. Conservation tracking. In *IEEE Conference on Computer Vision and Pattern Recognition*, pages 2928–2935, 2013. 1, 2
- [52] Uwe Schmidt, Martin Weigert, Coleman Broaddus, and Gene Myers. Cell detection with star-convex polygons. In *International Conference on Medical Image Computing and Computer-Assisted Intervention*, pages 265–273. Springer, 2018. 1, 6
- [53] Jianbo Shi and Jitendra Malik. Normalized cuts and image segmentation. *IEEE Transactions on Pattern Analysis and Machine Intelligence*, 22(8):888–905, 2000. 2
- [54] Ernst HK Stelzer, Frederic Strobl, Bo-Jui Chang, Friedrich Preusser, Stephan Preibisch, Katie McDole, and Reto Fiolka. Light sheet fluorescence microscopy. *Nature Reviews Methods Primers*, 1(1):73, 2021. 1
- [55] Carsen Stringer, Tim Wang, Michalis Michaelos, and Marius Pachitariu. Cellpose: a generalist algorithm for cellular segmentation. *Nature Methods*, 18(1):100–106, 2021. 1, 6
- [56] Ko Sugawara, Çağrı Çevrim, and Michalis Averof. Tracking cell lineages in 3d by incremental deep learning. *eLife*, 11:e69380, 2022. 1, 2, 3, 7
- [57] Mingxing Tan and Quoc Le. Efficientnet: Rethinking model scaling for convolutional neural networks. In *International Conference on Machine Learning*, pages 6105–6114, 2019. 1
- [58] Robert Endre Tarjan. Efficiency of a good but not linear set union algorithm. *Journal of the ACM (JACM)*, 22(2):215–225, 1975. 4
- [59] Engin Türetken, Xinchao Wang, Carlos J Becker, Carsten Haubold, and Pascal Fua. Network flow integer programming to track elliptical cells in time-lapse sequences. *IEEE Transactions on Medical Imaging*, 36(4):942–951, 2016. 1, 2, 3, 7
- [60] Vladimír Ulman, Martin Maška, Klas EG Magnusson, Olaf Ronneberger, Carsten Haubold, Nathalie Harder, Pavel Matula, Petr Matula, David Svoboda, Miroslav Radojevic, et al. An objective comparison of cell-tracking algorithms. *Nature Methods*, 14(12):1141–1152, 2017. 2, 5, 8, 12
- [61] Stefan Van der Walt, Johannes L Schönberger, Juan Nunez-Iglesias, François Boulogne, Joshua D Warner, Neil Yager, Emmanuelle Gouillart, and Tony Yu. scikit-image: image processing in python. *PeerJ*, 2:e453, 2014. 6
- [62] Pauli Virtanen, Ralf Gommers, Travis E Oliphant, Matt Haberland, Tyler Reddy, David Cournapeau, Evgeni Burovski, Pearu Peterson, Warren Weckesser, Jonathan Bright, et al. Scipy 1.0: fundamental algorithms for scientific computing in python. *Nature Methods*, 17(3):261–272, 2020. 5, 6
- [63] Saining Xie and Zhuowen Tu. Holistically-nested edge detection. In *IEEE Conference on Computer Vision and Pattern Recognition*, pages 1395–1403, 2015. 7
- [64] Bin Yang, Merlin Lange, Alfred Millett-Sikking, Xiang Zhao, Jordão Bragantini, Shruthi Vijay Kumar, Mason Kamb, Rafael Gómez-Sjöberg, Ahmet Can Solak, Wanpeng Wang, et al. Daxi—high-resolution, large imaging volume and multi-view single-objective light-sheet microscopy. *Nature Methods*, 19(4):461–469, 2022. 2, 8
- [65] Julian Yarkony, Alexander Ihler, and Charless C Fowlkes. Fast planar correlation clustering for image segmentation. In *European Conference on Computer Vision*, pages 568–581. Springer, 2012. 2
- [66] Andy B Yoo, Morris A Jette, and Mark Grondona. SLURM: Simple linux utility for resource management. In *Job Scheduling Strategies for Parallel Processing: 9th International Workshop*, pages 44–60. Springer, 2003. 8
- [67] Christophe Zimmer, Elisabeth Labruyere, Vannary Meas-Yedid, Nancy Guillén, and J-C Olivo-Marin. Segmentation and tracking of migrating cells in videomicroscopy with parametric active contours: A tool for cell-based drug testing. *IEEE Transactions on Medical Imaging*, 21(10):1212–1221, 2002. 2

A Content

This supplementary document presents additional information about our setup for the quantitative experiment on the cell tracking challenge (CTC) [60] and how the perturbed hierarchies impact different datasets.

B CTC Quantitative comparison

B.1 Processing details

Here we describe in detail our CTC submission (Section 4.2).

All datasets were linearly interpolated on the z-axis to make them isotropic. They were normalized by their lower and upper quantiles (lq and uq in Table 3), DRO dataset had corrupted voxels which were set to 0.

In the datasets MDA231 and CE, where 3D segmentation labels are available, we trained a U-Net to predict the foreground and the cell boundaries. In the DRO and TRIC datasets, where 3D labels are not available, we tried two different approaches:

- IM: where the cells and their contours were estimated using traditional image processing operators;
- PL: where we trained the U-Nets on labels generated by an algorithm and not manually annotated.

Both PL and IM processing began the same way. The cells were detected using a difference of Gaussians with σ_1 and σ_2 thresholding at 0.5 and 0.75 times their Otsu, for DRO and TRIC, respectively. The cell contour maps were simply the inverse of the Gaussian blurred image with σ_1 and normalized to be between 0 and 1. Through visual inspection, we selected $\sigma_1 = 2$ and $\sigma_2 = 8$ for the DRO dataset and $\sigma_1 = 1$ and $\sigma_2 = 6$ for the TRIC dataset, the two bottom and top z-planes from TRIC were ignored during processing because some contained excessive artifacts. For the pseudo-labels, we used these contour maps and detections to run the hierarchical watershed and performed a horizontal cut in the hierarchy to obtain the flat segments used for training the network. In IM, they were used as the tracking input.

For the training set, the normalized time lapses were used to learn the network weights and find the optimal hyper-parameters using grid search and cross-validation between datasets. For that, we trained a network in a single dataset and computed the results on the other. For example, we trained on dataset 01 and predicted the network outputs, tracked, and measured the accuracy on dataset 02.

The parameter power p of the ILP weights (w^p) was fixed to 4 throughout the experiments.

The U-Nets were trained for 20 epochs using a learning rate of 10^{-4} with exponential weight decay of 0.95 at every epoch. The networks used a kernel size of 5, with

simple convolution blocks without residual connections or batch normalization. The number of planes used were 32, 64, 128, and 256. The network features are linearly interpolated in the up-sampling step of the U-Net decoder. The best parameters found through the grid search are reported in Table 3.

The images are processed in tiles with overlap to avoid boundary artifacts of the CNNs' inference. Once a whole frame was computed, the foreground detection channels were binarized with a *Threshold* parameter, and the contours were gaussian blurred with σ , values at Table 3. The PL and IM approaches shared the same parameters.

For the final submission, both training datasets were used for learning the weights, and the segmentation and tracking were done using the hyper-parameters found on the training sets as described above.

B.2 Cross-validation results

Table 4 reports our cross-validation results on the training set from Section 4.2 from the main text.

The image processing solution showed superior results than the pseudo-labels alternative in both DRO and TRIC datasets. Hence, it was the regime used in the final submission. Notably, the gap in evaluation metrics is the largest in the extremely challenging DRO dataset, where existing solutions achieve a low score when compared to other datasets. This is one of the datasets we achieved the top score in the hidden test set (Table 2 from the main text).

C Perturbed hierarchy results

In this section, we analyze the usage of the perturbed hierarchy construction proposed in Section 3.2 of the main text.

Figure 7 shows the average results of 3 runs of probing the cell contours of the datasets from the CTC with an increasing amount of uniform random noise and how that affects their performance.

In the CE dataset, where the cells are not very motile, and spurious segments with high IoU are more likely to happen, it shows a significant increase in accuracy. In the DRO dataset, there is an average increase in both the PL and IM regimes, despite working much better in dataset 02. As expected, the benefits decrease at some point. In the other two datasets, MDA231 and TRIC, the accuracy fluctuates, and it does not indicate a clear improvement. In these datasets, the cells are more motile, so the scenario of overlapping spurious regions where the additive noise is beneficial is less likely to happen.

Dataset	normalization		CNN output		hierarchy construction				tracking			
	lq	uq	σ	Threshold	Min. Area	Max. Area	Contour Strength	Noise	Link Radius	w_α	w_β	w_δ
MDA231	0.001	0.9999	0.5	0.5	2500	25000	0.2	0	75	-0.01	-0.01	-0.001
CE	0.001	0.9999	1	0.1	5000	1000000	0	0.4	100	-0.005	-0.005	0
DRO	0.001	0.9999	1	0.5	1500	50000	0.1	0.1	50	-0.001	-0.001	-0.001
TRIC	0.05	0.999	2	0.5	500	7500	0	0.1	50	-0.01	-0.001	0

Table 3: Table of parameters used for our cell tracking challenge submission.

Dataset	Regime	File	TRA	SEG	CTB
MDA231	Sup	1	0.888	0.613	0.751
		2	0.923	0.626	0.774
		AVG	0.905	0.620	0.763
CE	Sup	1	0.970	0.705	0.838
		2	0.955	0.649	0.802
		AVG	0.963	0.677	0.820
DRO	PL	1	0.693	0.425	0.559
		2	0.923	0.528	0.726
		AVG	0.808	0.476	0.642
DRO	IM	1	0.812	0.512	0.662
		2	0.934	0.556	0.745
		AVG	0.873	0.534	0.704
TRIC	PL	1	0.946	0.552	0.749
		2	0.880	0.690	0.785
		AVG	0.913	0.621	0.767
TRIC	IM	1	0.980	0.527	0.754
		2	0.853	0.733	0.793
		AVG	0.917	0.630	0.773

Table 4: Results on the training set of the cell tracking challenge; Fully supervised (Sup) and pseudo-labels (PL) regimes used cross-validation; Image processing (IM) does not require training and achieved better results, especially on the DRO dataset.

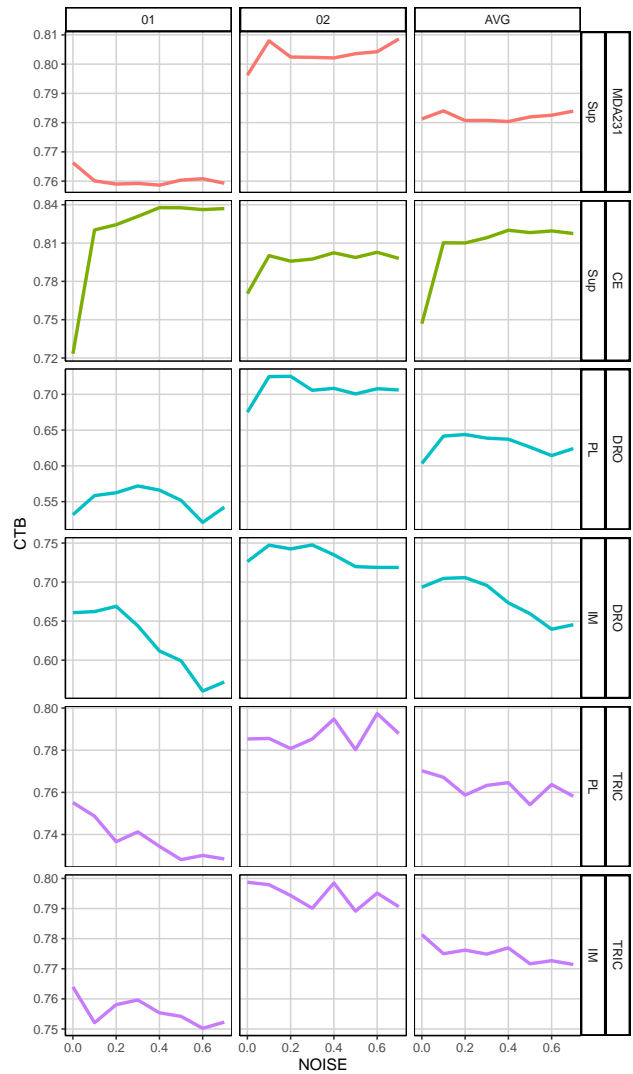


Figure 7: Relationship between CTB score and amount of uniform random noise added to the contour map; columns indicate different images and their average; rows, different datasets, and inputs; and color also indicates datasets.